Nano Research 2018, 11(5): 2450–2459
https://doi.org/10.1007/s12274-017-1866-y
Research Article
ISSN 1998-0124
CN 11-5974/O4

Polarized few-layer g-C_3N_4 as metal-free electrocatalyst for highly efficient reduction of CO_2

Bing Zhang, Tian-Jian Zhao, Wei-Jie Feng, Yong-Xing Liu, Hong-Hui Wang, Hui Su, Li-Bing Lv, Xin-Hao Li (✉), and Jie-Sheng Chen (✉)

School of Chemistry and Chemical Engineering, Shanghai Jiao Tong University, Shanghai 200240, China

Received: 31 July 2017
Revised: 21 September 2017
Accepted: 22 September 2017

KEYWORDS
CO_2 reduction,
two-dimensional (2D) materials,
metal-free electrocatalyst,
electrochemistry,
nanostructures

ABSTRACT

The greenhouse effect and global warming are serious problems because the increasing global demand for fossil fuels has led to a rapid rise in greenhouse gas exhaust emissions in the atmosphere and disruptive changes in climate. As a major contributor, CO_2 has attracted much attention from scientists, who have attempted to convert it into useful products by electrochemical or photoelectrochemical reduction methods. Facile design of efficient but inexpensive and abundant catalysts to convert CO_2 into fuels or valuable chemical products is essential for materials chemistry and catalysis in addressing global climate change as well as the energy crisis. Herein, we show that two-dimensional few-layer graphitic carbon nitride (g-C_3N_4) can function as an efficient metal-free electrocatalyst for selective reduction of CO_2 to CO at low overpotentials with a high Faradaic efficiency of ~ 80%. The polarized surface of ultrathin g-C_3N_4 layers (thickness: ~ 1 nm), with a more reductive conduction band, yields excellent electrochemical activity for CO_2 reduction.

1 Introduction

Reduction of CO_2 to fuels over both homogeneous and heterogeneous catalysts has been widely studied [1–9]. Among these strategies [4–8] for activating and reducing CO_2 molecules, the electrocatalytic process using heterogeneous electrocatalysts was believed to be a more direct and efficient path [10, 11]. Despite considerable efforts, rational designing of efficient electrocatalysts, especially inexpensive and sustainable metal-free electrocatalysts, remains a scientifically challenging problem. There is consensus that fixation of CO_2 molecules on active sites and an appropriate energy input are the main steps for CO_2 reduction over an electrocatalyst [12]. The selectivity to certain products, such as carbon monoxide, formic acid, methanol, and other hydrogen carbons, is largely determined by the electronic structure, more precisely by the formal potentials of the electrocatalyst and also its surface functional groups. For example, heteroatom doping or an ionic liquid molecule coating were applied to modify the structure of nanocarbons, e.g.,

Address correspondence to Xin-Hao Li, xinhaoli@sjtu.edu.cn; Jie-Sheng Chen, chemcj@sjtu.edu.cn

nanodiamonds, graphene, and nanotubes, and boost their activity for CO_2 reduction [13–17]. Pioneering works indicated significant potential for further engineering of the structure and chemistry of carbonaceous materials into more efficient metal-free electrocatalysts for CO_2 conversion [12, 18].

Materials based on graphitic carbon nitride (g-C_3N_4), the most stable phase among all the allotropes of carbon nitride, have attracted much attention owing to their wide applications as sustainable heterogeneous catalysts for artificial photosynthesis, electrocatalysis, and organic catalysis [19–26]. Mesoporous g-C_3N_4 was also used as a heterogeneous catalyst to activate CO_2 for the oxidation of benzene to phenol at elevated temperatures [18]. Theoretical studies and experimental results also suggested that modified g-C_3N_4 has an appropriate energy potential for CO_2 reduction. Recently, g-C_3N_4-based nanomaterials were also applied as electrocatalysts for the hydrogen evolution reaction (HER) or oxygen evolution reaction [23, 24]. However, electrochemical reduction of CO_2 over metal-free g-C_3N_4 has not been reported in the literature. Further modification of the band structure and morphology of g-C_3N_4 materials is highly desired to boost the catalytic performance for electrocatalytic reduction of CO_2, especially to valuable chemical products, and to simultaneously suppress the HER.

Herein, we report the development of a metal-free g-C_3N_4-based electrocatalyst for selective CO_2 reduction to CO. A polarized ultrathin g-C_3N_4 layer (thickness: ~ 1 nm) was prepared on a large scale by a hydrothermal–thermal exfoliation method. The polarized surface and modified electronic structure induced by the ultrathin nanostructure yield high activity and stability in two-dimensional (2D) polarized g-C_3N_4 (2D-pg-C_3N_4) for CO_2 reduction in $KHCO_3$ electrolyte.

2 Experimental section

2.1 Materials

Dicyandiamide (DCDA) (Acros Organics, 99.5%), potassium hydrogen carbonate (Adamas Reagent Co., Ltd., 99%), dimethyl sulfoxide (DMSO, Aladdin, 99.9%), D_2O (Adamas Reagent Co., Ltd., 99.9%), ethanol (HPLC grade, Adamas Reagent Co., Ltd., 99.8%), and formic acid (Aladdin, 95%) were used as received. The Nafion® perfluorinated resin solution (5 wt.% in lower aliphatic alcohols and water; contains 15%–20% water) was purchased from Sigma-Aldrich.

2.2 Preparation of 2D-pg-C_3N_4 layers consisting of g-C_3N_4 foam

DCDA (4 g) was dissolved in 100 mL of deionized water under sonication for 10 min. The solution was sealed in a Teflon™-lined autoclave and heated at 190 ˚C for 4 h. Liquid nitrogen was used to induce freezing-assisted assembly, and the freeze-dried samples were further heated at 550 ˚C for 4 h at a ramp rate of 2.3 ˚C/min in an N_2 atmosphere to obtain porous g-C_3N_4. Then 2D-pg-C_3N_4 layers consisting of g-C_3N_4 foam were obtained by further thermal exfoliation of the as-obtained porous g-C_3N_4 at 400 ˚C for 2 h in air.

2.3 Preparation of bulk g-C_3N_4

Bulk g-C_3N_4 was prepared by direct calcination of the DCDA powder at 550 ˚C in an N_2 atmosphere. After cooling naturally to room temperature, the as-obtained samples were used for further study and characterization.

2.4 Preparation of mesoporous g-C_3N_4

Mesoporous g-C_3N_4 (mpg-C_3N_4) samples were prepared according to our previous report [22]. Namely, 5 g of cyanamide was dissolved in 7.5 g of Ludox HS40 solution (dispersion of 40 wt.% of 12 nm SiO_2 particles in water) and heated at 65 ˚C overnight to remove water. The as-obtained white powder was heated at 600 ˚C for 4 h (ramp rate: 2.3 ˚C/min) under an N_2 atmosphere. The resulting brown-yellow powder was treated with 4 M HF acid for 24 h to remove the silica template. The powders were then centrifuged and washed three times with distilled water and twice with ethanol. Finally, the powders were dried at 60 ˚C under vacuum overnight.

2.5 Electrochemical measurements

The electrochemical HER activities of 2D-pg-C_3N_4 and control samples were measured using the rotating

disc electrode (RDE) technique. Samples (1 mg) were dispersed in a mixed solution containing 80 μL of a 5 wt.% Nafion® solution in alcohol, 350 μL of water, and 750 μL of ethanol. The working electrode was prepared by transferring ink onto a glassy carbon RDE (5 mm in diameter; PINE Instruments, USA). Electrochemical tests were performed on a CHI 660C electrochemical workstation. A typical three-electrode system was used to conduct all the following electrochemical tests. A platinum wire was used as a counter electrode, and an Ag/AgCl electrode in saturated KCl solution was used as the reference electrode.

2.6 Electrochemical CO_2 reduction reaction test

A 2 M $KHCO_3$ aqueous solution was used as the electrolyte. Cyclic voltammetry (CV) measurements were made at 50 mV/s from −0.4 to −1.5 V for 100 cycles in the above gas-saturated electrolyte. Linear scanning voltammetry (LSV) measurements were made using the RDE in CO_2- or N_2-saturated electrolytes at a sweep rate of 10 mV/s.

2.7 Faraday efficiency calculation

The liquid products were quantified by ^{1}H nuclear magnetic resonance (NMR) spectroscopy, in which 0.5 mL of electrolyte (a total of 100 mL in the reactor) was mixed with 0.1 mL of D_2O, and 0.05 μL of DMSO was added as an internal standard. An electrolyte (0.5 mL) containing 10 μL of formic acid was used as the standard to verify the chemical shift of $HCOO^-$ species and facilitate quantification of the amount of formic acid in the liquid products by calculating the factor X in the equation $n_F/n_D \times X = A_F/A_D$, where n_F is the molarity of formic acid, n_D is the molarity of DMSO, and A_F and A_D are the integrated areas of the ^{1}H spectrum corresponding to $HCOO^-$ and DMSO, respectively. After the factor X is verified, the molarity of $HCOO^-$ species in liquid products can also be calculated. Further, the gas-phase products (n_{CO}, n_{H2}) were determined by gas chromatography (GC, Shimadzu Co., Ltd.) with a thermal conductivity detector and flame ionization detector. Then the Faraday efficiency (FE) can be calculated as FE = $nN \times 96500/[(It) \times (60/0.5)]$, where N is the electron number for the HER or CO_2 reduction to CO and $HCOO^-$ (here, N is 2); n represents n_{CO}, n_{H2}, or n_F; I is the current (A); and t represents time (s).

2.8 Characterization

Scanning electron microscopy (SEM) measurements were performed on a FEI Nova NanoSEM 2300. Transmission electron microscopy (TEM) and high-resolution TEM (HRTEM) measurements were obtained using a JEM-2100F microscope operated at an acceleration voltage of 200 kV. Atomic force microscopy (AFM) tests were conducted with a Nanonavi E-Sweep Scanning Probe Microscope. The powder X-ray diffraction (XRD) patterns were recorded on a Bruker D8 Advance X-ray diffractometer with Cu-Kα radiation (λ = 1.5418 Å) at a scan rate of 6 °/min. UV–vis spectra were recorded with a Shimadzu UV-2450 UV–vis spectrophotometer.

3 Results and discussion

3.1 Structural characterizations

Among all the methods for preparing g-C_3N_4 nanosheets, concentrated acid exfoliation [25] and sonication in a polar solvent [26] are the two main methods described in literature. Although the excellent performance of thin g-C_3N_4 nanosheets in biological imaging, photocatalysis, and the water splitting reaction has been well demonstrated in pioneering works, mass production of ultrathin g-C_3N_4 nanosheets remains a significant challenge. The use of large amounts of concentrated acid is inconvenient and unsafe for real applications. Protonation is also inevitable, as both the chemical and electronic structures change during the acid exfoliation process. Long-time sonication of bulk g-C_3N_4, which has low yields, is not efficient enough for mass production of g-C_3N_4 thin layers. Moreover, because of their 2D structure with a very large aspect ratio, ultrathin g-C_3N_4 nanosheets easily aggregate and are packed into bulk phases during sample separation and reaction. As a result, we chose to construct three-dimensional (3D) monoliths composed of ultrathin g-C_3N_4 nanosheets, which are expected to have high mechanical stability for practical uses, including use as a metal-free electrocatalyst for CO_2 reduction here.

Porous but rigid g-C_3N_4 nanoassemblies (Fig. S1 in the Electronic Supplementary Material (ESM)) were prepared via a modified monomer preorganization method from DCDA. The mechanical properties of the g-C_3N_4 nanoassemblies obviously changed after thermal exfoliation. The as-fabricated 2D-pg-C_3N_4 became flexible (Fig. S2 in the ESM) and lightweight, with a density of 5.5 mg/cm^3 (Fig. 1(a) and Fig. S3 in the ESM). Large-area SEM images (Fig. 1(b) and Fig. S4 in the ESM) revealed that the 2D-pg-C_3N_4 was obtained as monoliths of continuous but entangled nanosheets, whereas the bulk sample showed a condensed layer structure (Fig. S5 in the ESM). The detailed morphological characteristics of the primary g-C_3N_4 nanosheets were revealed by further TEM analysis (Fig. 2(c) and Fig. S6 in the ESM), confirming their uniform 2D structure and ultralow thickness (less than 3 nm; Fig. 1(d)). Because of the extremely low thickness of the primary subunits, the 2D-pg-C_3N_4 was easily torn into small pieces under mild ultrasonication within 50 s and was well dispersed in water (Fig. S7 and Movie S1 in the ESM). AFM analysis (Fig. 1(e)) of the dispersed 2D-pg-C_3N_4 on a mica substrate demonstrated the ultrathin 2D nature of the primary g-C_3N_4 nanosheets, which had an average thickness of 1 nm. The 2D-pg-C_3N_4 can also be expected to have a high surface area, and the surface area was calculated to be 292.4 m^2/g from the nitrogen adsorption/desorption analysis results (Fig. 2(b) and Fig. S8 in the ESM).

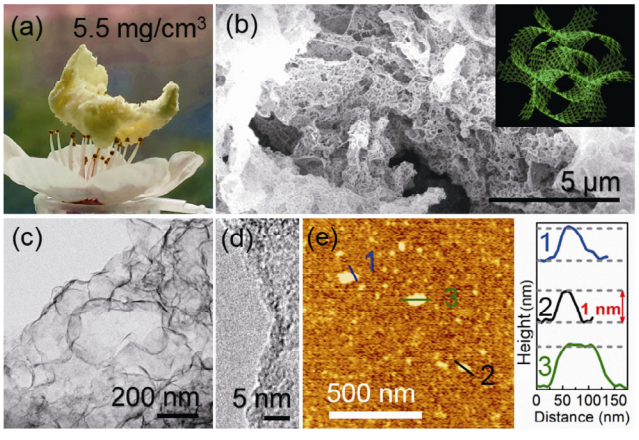

Figure 1 Morphology of g-C_3N_4 monolith composed of 2D-pg-C_3N_4. Photograph (a), SEM image (b), TEM image (c), and HRTEM image (d) of the g-C_3N_4 monolith, and AFM analysis results (e) for the primary 2D-pg-C_3N_4 layers making up the g-C_3N_4 monolith. Inset in (b): schematic structure of the few-layer 2D-pg-C_3N_4.

Thermally exfoliated 2D-pg-C_3N_4 is thought to possess the characteristics of bulk g-C_3N_4, with some differences caused by its nanostructure. The XRD patterns of the 2D-pg-C_3N_4 sample revealed good development of the crystalline structure of graphitic carbon nitride (Fig. 2(a)). The relatively broad peak at 27.3° for the 2D-pg-C_3N_4 indicated only limited stacking in the *c* direction of the graphitic carbon nitride structure, which is also reflected by the less pronounced peak at 13.1°, originating from planar ordering parallel to the *c* axis [19, 26]. Fourier transform infrared (FTIR) spectroscopy (Fig. 2(c)) further demonstrated the similar chemical structures of the foam and bulk samples. The peak of the heptazine ring breathing mode at approximately 810 cm^{-1} and the peaks originating from either the trigonal C–N=C (full condensation) or bridging C–NH–C group stretching mode in the region of 900 to 1,800 cm^{-1} became sharper compared with those of bulk g-C_3N_4 in the FTIR spectra of 2D-pg-C_3N_4, suggesting an even condensed polymeric network [20, 26]. The thermal exfoliation process obviously helped remove the distorted and less condensed basic units, liberate the highly crystalline thin layers, and thus generate an even flexible nanofoam. Despite slight changes in the chemical structure, the band gap of the 2D-pg-C_3N_4 became even broadened and was estimated to be 2.88 eV, which was 0.15 eV larger than that of the bulk sample, as calculated from the UV–vis absorption spectra (Fig. 2(d)). The changed band structure is believed to be relevant to the redox ability of materials for electrocatalytic reactions.

3.2 Electrochemical characterization

Our initial studies focused on the electrochemical reduction of CO_2 in $KHCO_3$ solution. LSV curves (Figs. 3(a) and 3(b)) of 2D-pg-C_3N_4 and control samples were obtained in a three-electrode system at a scan rate of 10 mV/s in 2 M $KHCO_3$ saturated with N_2 (HER process) or CO_2. As revealed by the LSV curves of the 2D-pg-C_3N_4 measured in the N_2- and CO_2-saturated electrolytes (Fig. 3(a)), the significantly enhanced current density after CO_2 flow directly demonstrated that reduction of CO_2 proceeds over the 2D-pg-C_3N_4-based working electrode. As control samples, bulk g-C_3N_4 and bare glassy carbon provided

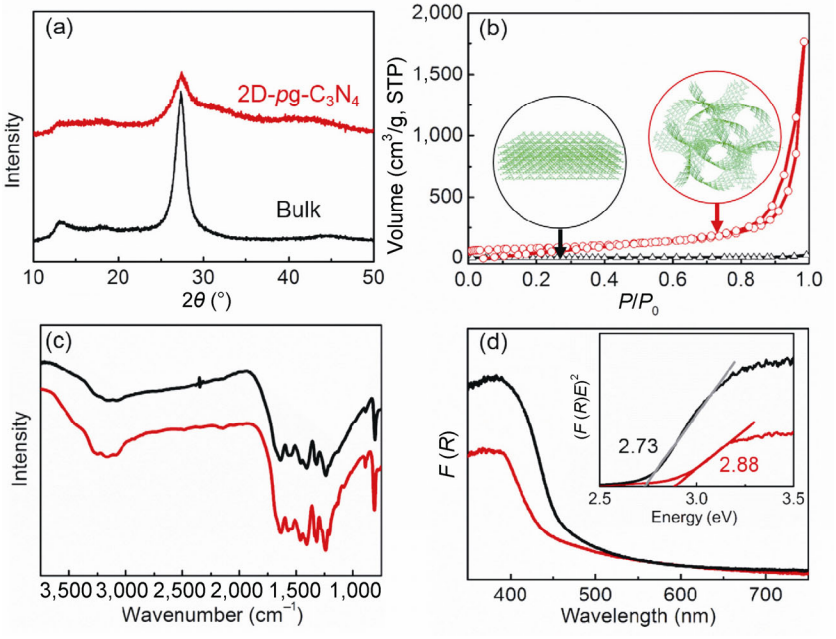

Figure 2 Structural characteristics of 2D-pg-C_3N_4. XRD patterns (a), nitrogen adsorption/desorption isotherms (b), FTIR spectra (c), and UV–vis absorption spectra (d) of 2D-pg-C_3N_4 and bulk samples. Insets: schematic structures (b) and Kubelka–Munk plots (d) of the 2D-pg-C_3N_4 and bulk samples.

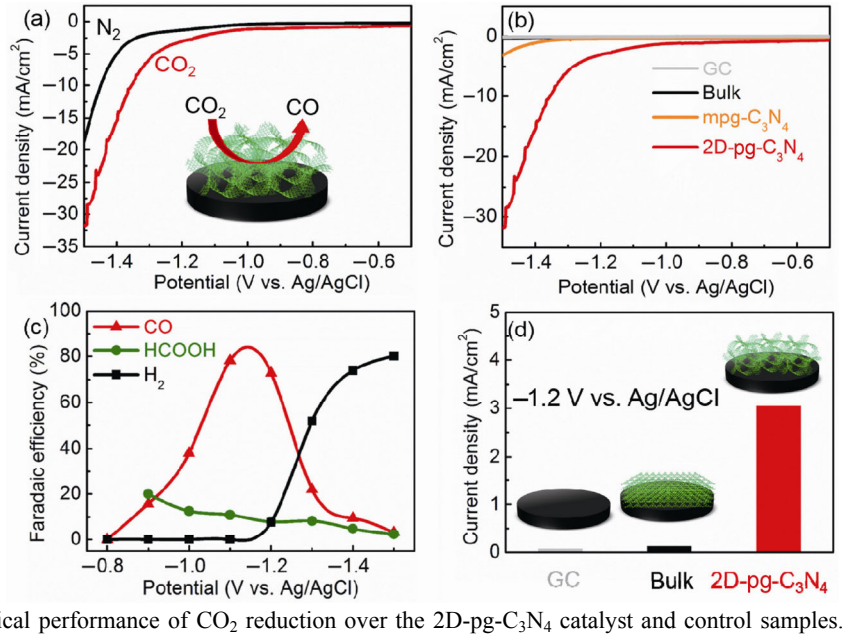

Figure 3 Electrochemical performance of CO_2 reduction over the 2D-pg-C_3N_4 catalyst and control samples. LSV curves in N_2- and CO_2-saturated 2 M $KHCO_3$ solutions (a) and Faradaic efficiency at different voltages for 12 h (c) of the 2D-pg-C_3N_4 catalyst for CO_2 reduction; LSV curves (b) and corresponding current densities at −1.2 V vs. Ag/AgCl (d) of the 2D-pg-C_3N_4 and control samples in CO_2-saturated 2 M $KHCO_3$ solution.

only negligible to low current density at the same working voltage for a 2D-pg-C_3N_4 catalyst in the CO_2-saturated electrolyte (Fig. 3(b) and Fig. S9(a) in the ESM). Further, the precursor of the 2D-pg-C_3N_4 sample without thermal exfoliation (Fig. S10 in the ESM) also showed weak performance in the CO_2-saturated electrolyte compared with the 2D-pg-C_3N_4 electrocatalyst (Fig. S9(b) in the ESM). The 2D-pg-C_3N_4 exhibited the best CO_2 reduction activity among all the samples tested here, with an onset potential of −0.9 V vs.

Ag/AgCl (η_{CO} = −0.77 V) (Fig. 3(a)). The current density achieved by the 2D-pg-C_3N_4 at −1.2 V vs. Ag/AgCl is 3.05 mA/cm^2, which is nearly 30 times larger than that over the bulk g-C_3N_4 catalyst (Fig. 3(d)).

Note that the precursor used to prepare the g-C_3N_4 samples was of ultrahigh purity. Highly pure water and solvents were also used in this work for materials synthesis. We conducted inductively coupled plasma emission spectrometry tests of g-C_3N_4 samples (Table S2 in the ESM), which excluded the possibility of the presence of even a trace amount of metal elements (below the ppm level) in our g-C_3N_4 foams. Moreover, the effect of an undetectable amount of metals on the CO_2 reduction activity of the samples is negligible, as is well demonstrated by the poor activity (Fig. 3(b)) of the bulk samples and mesoporous versions made from the same precursor.

The selectivity of the 2D-pg-C_3N_4 catalyst for CO_2 reduction was further investigated by analyzing the gas-phase and liquid-phase products. Then *I*–*t* curves were obtained for 12 h to verify the occurrence of electrochemical CO_2 reduction. ^{1}H NMR spectral analysis demonstrated complete conversion of CO_2 to $HCOO^-$ with a chemical shift at 8.3 ppm (Fig. S11 in the ESM). Further, the gas-phase products were analyzed by GC. The Faradaic efficiency for the formation of CO (FE_{CO}) over the 2D-pg-C_3N_4 catalyst increased from 15.7% to ~ 80% with increasing voltage from −0.9 to −1.1 V vs. Ag/AgCl (Fig. 3(c)). Moreover, formation of formic acid over the 2D-pg-C_3N_4 catalyst was also confirmed by ^{1}H NMR analysis of the solution-phase products, which had Faradaic efficiencies between 20% and 11% at −0.9 to −1.1 V vs. Ag/AgCl (Fig. S12 in the ESM). As the main counterpart reaction, the HER was largely suppressed over the 2D-pg-C_3N_4 catalyst at low potentials (< −1.15 V vs. Ag/AgCl). Surprisingly, the total Faradaic efficiency for the conversion of CO_2 over the metal-free 2D-pg-C_3N_4 catalyst was about 91% at applied voltages between −1.05 and −1.15 V vs. Ag/AgCl, which is comparable to or even better than the reported values of state-of-the-art catalysts, including metal-free and based catalysts (Table S1 in the ESM) [4, 6, 8, 27–32]. These results illustrated well the outstanding electrochemical CO_2 reduction performance of 2D-pg-C_3N_4 as a metal-free catalyst (Table S2 in the ESM). The source of CO and formic acid was also investigated using GC to analyze the possible gas products in the presence and absence of CO_2 gas. The fact that CO was not detected without the introduction of CO_2 into the $KHCO_3$ solution demonstrated the formation of CO from CO_2 reduction, rather than reduction of the $KHCO_3$, in our catalytic system (Fig. S13 in the ESM). Moreover, formic acid was also not observed by NMR in the absence of CO_2 gas. All these results demonstrated well that CO_2 was the only source for the formation of both CO and formic acid [4, 32].

3.3 Mechanism of CO_2 reduction on 2D-pg-C_3N_4 nanolayers

The large surface area and porous structure could not ensure high activity of the g-C_3N_4-based electrocatalysts for CO_2 reduction. The hierarchical structure of the foam-like monolith composed of 2D-pg-C_3N_4 with a large surface area also facilitates diffusion of CO_2 molecules to the active surface of the catalyst. The improved mass transfer efficiency of the 2D-pg-C_3N_4 is revealed by the electrochemical impedance spectra of the 2D-pg-C_3N_4 (Fig. S14 in the ESM), which exhibit a larger slope in the low-frequency range and thus an even lower mass diffusion resistance for further CO_2 reduction reactions. A benchmarked photocatalyst reported in the literature [22, 33, 34], mpg-C_3N_4, which also has a larger surface area but the same band structure as bulk g-C_3N_4, has been widely used as an efficient catalyst or photocatalyst for organic synthesis and water splitting reactions. For the CO_2 reduction reaction tested in our system, mpg-C_3N_4 exhibited only negligible improvement in the onset overpotential (Fig. 3(b)), although the current output was more or less elevated at high overpotentials, again owing to the improved mass transfer efficacy obtained by introducing nanopores. The remarkably enhanced reducing power of the 2D-pg-C_3N_4, which presumably results from the formation of an ultrathin layered structure, is believed to significantly depress the onset overpotential for CO_2 reduction here. Indeed, temperature-programmed desorption (TPD) tests using CO_2 as the probe molecule (Fig. 4(b)) indicated an even lower CO_2 desorption peak for the 2D-pg-C_3N_4 than for the bulk sample, suggesting a more favorable activation process over 2D-pg-C_3N_4 for possible

reduction of CO_2 molecules [35–37].

The key role of the ultrathin structure of g-C_3N_4 layers for promoting CO_2 reduction was also demonstrated by monitoring possible changes in the electronic structure. Engineering carbon nitride materials into ultrathin layers obviously changed the electronic structure of g-C_3N_4 (Figs. 4(c)–4(e)), which has already been revealed by the UV–vis absorption spectra (Fig. 2(d)) of the 2D-pg-C_3N_4 and bulk samples. More importantly, the ultrathin 2D structure provides the g-C_3N_4 layers with a polarized surface with enhanced electron enrichment. X-ray photoelectron spectroscopy (XPS) N 1s and C 1s spectra (Figs. 4(d) and 4(e)) revealed obvious shifts of the characteristic peaks of sp^2 N (at 398.4 eV, Fig. 4(d)) and C (at 288.0 eV, Fig. 4(e)) atoms to lower binding energies, suggesting an enhanced electron density of aromatic rings in the ultrathin g-C_3N_4 layers. Note that the typical peaks of sp^2 C–C bonds of graphitic carbon at 284.6 eV, which generally appeared in all the g-C_3N_4 samples in the literature [38–40], are the same for both the 2D-pg-C_3N_4 and bulk samples. XPS valence band spectra (Fig. 4(c)) demonstrated that the valence band position is 1.18 eV, which is nearly 0.38 eV more negative than that of the bulk samples (1.56 eV). Only the C and N atoms in the conjugated C=N–N system of triazine shifted to lower binding energies compared with those of the bulk samples, presumably owing to the quantum effect originating from the ultrathin 2D structure [41]. As a result, the 2D-pg-C_3N_4 showed a more reductive conduction band edge at −1.70 eV (Fig. 2(d)) compared with that of the bulk sample at −1.17 eV. These polarized melem subunits of the 2D-pg-C_3N_4 material, which have been proposed as active sites for electrochemical reduction of CO_2 molecules to useful fuels [8], seem to significantly boost its activity.

The role of the polarized melem subunits as active centers to promote CO_2 reduction over metal-free g-C_3N_4 was further illustrated by the corresponding Tafel plots (Fig. S15 in the ESM). The Tafel slope (161 mV/dec) obtained with the 2D-pg-C_3N_4 catalyst was consistent with a mixed mechanism, presumably a one-electron charge transfer from the catalyst to form $CO_2^{\bullet-}$ as the rate-determining process [42, 43]. In contrast, the large Tafel slope (321 mV/dec) of the bulk sample excluded the possibility of an electrocatalytic mechanism on its surface, where the physical CO_2 diffusion process dominated the reaction [44]. All of these results revealed that electrons are discharged more easily from the polarized melem subunits of the g-C_3N_4 nanosheets for further CO_2 reduction reactions. Although the more precise reaction mechanism awaits further study, the function of the electron-rich conjugated melem units, which is boosted by the ultrathin layered structure of 2D-pg-C_3N_4, in activating CO_2 by donating electrons is currently well-confirmed.

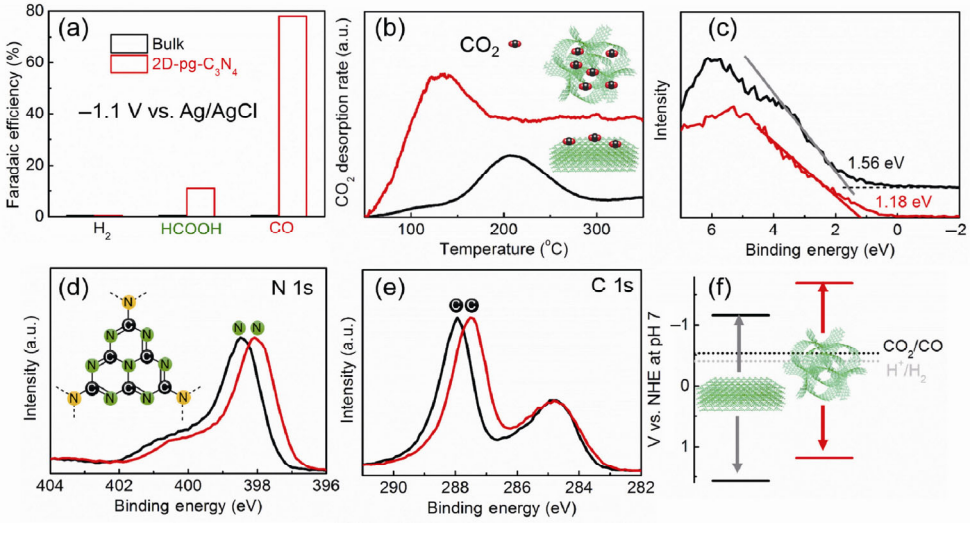

Figure 4 Roles of the 2D-pg-C_3N_4 nanolayers in CO_2 reduction. Faradaic efficiency at −1.1 V vs. Ag/AgCl (a), CO_2 TPD analysis results (b), XPS valence band spectra (c), XPS N 1s spectra (d), and XPS C 1s spectra (e) of the 2D-pg-C_3N_4 and bulk samples; (f) calculated band energy position of 2D-pg-C_3N_4 and bulk samples for possible electrochemical CO_2 reduction.

The 2D-pg-C_3N_4, which is based on the most stable allotrope of carbon nitride, also exhibited high electrochemical stability for CO_2 reduction. The *I*–*t* curve showed high durability of the 2D-pg-C_3N_4 catalyst for CO_2 reduction without an obvious loss of current density (~ 3 mA/cm^2) for more than 35,000 s (Fig. S16 in the ESM). The interconnected nanosheets in the foam-like monoliths could also maintain mechanical stability for long-term use in aqueous electrolytes. All the above features of the 2D-pg-C_3N_4 material illustrated its excellent potential for use as a sustainable and efficient catalyst for electrochemical reduction of CO_2 molecules to useful fuels.

4 Conclusion

In summary, we described a new electrocatalyst based on a metal-free g-C_3N_4 material for CO_2 reduction. We successfully engineered g-C_3N_4 into an interconnected monolith composed of 2D-pg-C_3N_4 to simultaneously boost the CO_2 reduction activity and improve the mass diffusion efficiency and mechanical stability. This metal-free electrocatalyst achieved a Faradaic efficiency of 91% at approximately −1.1 V vs. Ag/AgCl by selectively converting CO_2 to CO (~ 80%) and formic acid (~ 11%), and fully suppressing the HER process. Powerful inorganic and organic approaches are available for enhancing the electron transfer efficiency and modifying the ultrathin g-C_3N_4 layers, which are being considered as organic semiconductor nanosheets, indicating considerable potential for further facilitating the intrinsic activity of the g-C_3N_4-layer-based monoliths for selective conversion of CO_2 to specific hydrocarbon molecules. Our synthetic method also promises a general approach to preparing other functional carbon nitride nanosheets with significantly extended applications.

Acknowledgements

This work was supported by National Natural Science Foundation of China (Nos. 21331004, 21673140, and 21671134), Innovation Program of Shanghai Science and Technology Committee (No. 16JC1401600), Shanghai Eastern Scholar Program, Shanghai Rising-Star Program (No. 16QA1402100) and SJTU-MPI partner group.

Electronic Supplementary Material: Supplementary material (related methods, SEM and electrochemical data) is available in the online version of this article at https://doi.org/10.1007/s12274-017-1866-y.

References

[1] Kothandaraman, J.; Goeppert, A.; Czaun, M.; Olah, G. A.; Prakash, G. S. Conversion of CO_2 from air into methanol using a polyamine and a homogeneous ruthenium catalyst. *J. Am. Chem. Soc.* **2016**, *138*, 778–781.

[2] Pan, Y.-X.; Sun, Z.-Q.; Cong, H.-P.; Men, Y.-L.; Xin, S.; Song, J.; Yu, S.-H. Photocatalytic CO_2 reduction highly enhanced by oxygen vacancies on Pt-nanoparticle-dispersed gallium oxide. *Nano Res.* **2016**, *9*, 1689–1700.

[3] Wang, C. M.; Luo, X. Y.; Luo, H. M.; Jiang, D.-E.; Li, H. R.; Dai, S. Tuning the basicity of ionic liquids for equimolar CO_2 capture. *Angew. Chem., Int. Ed.* **2011**, *50*, 4918–4922.

[4] Gao, S.; Jiao, X. C.; Sun, Z. T.; Zhang, W. H.; Sun, Y. F.; Wang, C. M.; Hu, Q. T.; Zu, X. L.; Yang, F.; Yang, S. Y. et al. Ultrathin Co_3O_4 layers realizing optimized CO_2 electroreduction to formate. *Angew. Chem., Int. Ed.* **2016**, *55*, 698–702.

[5] Chen, Y. H.; Li, C. W.; Kanan, M. W. Aqueous CO_2 reduction at very low overpotential on oxide-derived Au nanoparticles. *J. Am. Chem. Soc.* **2012**, *134*, 19969–19972.

[6] Kondratenko, E. V.; Mul, G.; Baltrusaitis, J.; Larrazábal, G. O.; Pérez-Ramírez, J. Status and perspectives of CO_2 conversion into fuels and chemicals by catalytic, photocatalytic and electrocatalytic processes. *Energy Environ. Sci.* **2013**, *6*, 3112–3135.

[7] Sarkar, A.; Gracia-Espino, E.; Wågberg, T.; Shchukarev, A.; Mohl, M.; Rautio, A.-R.; Pitkänen, O.; Sharifi, T.; Kordas, K.; Mikkola, J.-P. Photocatalytic reduction of CO_2 with H_2O over modified TiO_2 nanofibers: Understanding the reduction pathway. *Nano Res.* **2016**, *9*, 1956–1968.

[8] Zhang, S.; Kang, P.; Ubnoske, S.; Brennaman, M. K.; Song, N.; House, R. L.; Glass, J. T.; Meyer, T. J. Polyethylenimine-enhanced electrocatalytic reduction of CO_2 to formate at nitrogen-doped carbon nanomaterials. *J. Am. Chem. Soc.* **2014**, *136*, 7845–7848.

[9] White, J. L.; Baruch, M. F.; Pander III, J. E.; Hu, Y.; Fortmeyer, I. C.; Park, J. E.; Zhang, T.; Liao, K.; Gu, J.; Yan, Y. et al. Light-driven heterogeneous reduction of carbon dioxide: Photocatalysts and photoelectrodes. *Chem. Rev.* **2015**, *115*, 12888–12935.

[10] Zhu, Q. G.; Ma, J.; Kang, X. C.; Sun, X. F.; Liu, H. Z.; Hu, J. Y.; Liu, Z. M.; Han, B. X. Efficient reduction of CO_2 into formic acid on a lead or tin electrode using an ionic liquid catholyte mixture. *Angew. Chem., Int. Ed.* **2016**, *128*, 9158–9162.

[11] Gao, S.; Lin, Y.; Jiao, X. C.; Sun, Y. F.; Luo, Q. Q.; Zhang, W. H.; Li, D. Q.; Yang, J. L.; Xie, Y. Partially oxidized atomic cobalt layers for carbon dioxide electroreduction to liquid fuel. *Nature* **2016**, *529*, 68–71.

[12] Kumar, B.; Asadi, M.; Pisasale, D.; Sinha-Ray, S.; Rosen, B. A.; Haasch, R.; Abiade, J.; Yarin, A. L.; Salehi-Khojin, A. Renewable and metal-free carbon nanofibre catalysts for carbon dioxide reduction. *Nat. Commun.* **2013**, *4*, 2819.

[13] Sato, S.; Morikawa, T.; Saeki, S.; Kajino, T.; Motohiro, T. Visible-light-induced selective CO_2 reduction utilizing a ruthenium complex electrocatalyst linked to a p-type nitrogen-doped Ta_2O_5 semiconductor. *Angew. Chem., Int. Ed.* **2010**, *49*, 5101–5105.

[14] Ge, J.-M.; Zhang, B.; Lv, L.-B.; Wang, H.-H.; Ye, T.-N.; Wei, X.; Su, J.; Wang, K.-X.; Li, X.-H.; Chen, J.-S. Constructing holey graphene monoliths via supramolecular assembly: Enriching nitrogen heteroatoms up to the theoretical limit for hydrogen evolution reaction. *Nano Energy* **2015**, *15*, 567–575.

[15] Rosen, B. A.; Salehi-Khojin, A.; Thorson, M. R.; Zhu, W.; Whipple, D. T.; Kenis, P. J. A.; Masel, R. I. Ionic liquid-mediated selective conversion of CO_2 to CO at low overpotentials. *Science* **2011**, *334*, 643–644.

[16] Mahurin, S. M.; Fulvio, P. F.; Hillesheim, P. C.; Nelson, K. M.; Veith, G. M.; Dai, S. Directed synthesis of nanoporous carbons from task-specific ionic liquid precursors for the adsorption of CO_2. *ChemSusChem* **2014**, *7*, 3284–3289.

[17] Zhang, B.; Wang, H.-H.; Su, H.; Lv, L.-B.; Zhao, T.-J.; Ge, J.-M.; Wei, X.; Wang, K.-X.; Li, X.-H.; Chen, J.-S. Nitrogen-doped graphene microtubes with opened inner voids: Highly efficient metal-free electrocatalysts for alkaline hydrogen evolution reaction. *Nano Res.* **2016**, *9*, 2606–2615.

[18] Goettmann, F.; Thomas, A.; Antonietti, M. Metal-free activation of CO_2 by mesoporous graphitic carbon nitride. *Angew. Chem., Int. Ed.* **2007**, *46*, 2717–2720.

[19] Wang, X. C.; Maeda, K.; Thomas, A.; Takanabe, K.; Xin, G.; Carlsson, J. M.; Domen, K.; Antonietti, M. A metal-free polymeric photocatalyst for hydrogen production from water under visible light. *Nat. Mater.* **2009**, *8*, 76–80.

[20] Han, Q.; Wang, B.; Zhao, Y.; Hu, C. G.; Qu, L. T. A graphitic-C_3N_4 "seaweed" architecture for enhanced hydrogen evolution. *Angew. Chem., Int. Ed.* **2015**, *54*, 11433–11437.

[21] Li, X.-H.; Chen, J.-S.; Wang, X. C.; Sun, J. H.; Antonietti, M. Metal-free activation of dioxygen by graphene/g-C_3N_4 nanocomposites: Functional dyads for selective oxidation of saturated hydrocarbons. *J. Am. Chem. Soc.* **2011**, *133*, 8074–8077.

[22] Cai, Y. Y.; Li, X. H.; Zhang, Y. N.; Wei, X.; Wang, K. X.; Chen, J. S. Highly efficient dehydrogenation of formic acid over a palladium-nanoparticle-based Mott–Schottky photocatalyst. *Angew. Chem., Int. Ed.* **2013**, *52*, 11822–11825.

[23] Ma, T. Y.; Dai, S.; Jaroniec, M.; Qiao, S. Z. Graphitic carbon nitride nanosheet-carbon nanotube three-dimensional porous composites as high-performance oxygen evolution electrocatalysts. *Angew. Chem., Int. Ed.* **2014**, *53*, 7281–7285.

[24] Liang, Q. H.; Li, Z.; Bai, Y.; Huang, Z.-H.; Kang, F. Y.; Yang, Q.-H. Reduced-sized monolayer carbon nitride nanosheets for highly improved photoresponse for cell imaging and photocatalysis. *Sci. China Mater.* **2017**, *60*, 109–118.

[25] Zhou, Z. X.; Wang, J. H.; Yu, J. C.; Shen, Y. F.; Li, Y.; Liu, A. R.; Liu, S. Q.; Zhang, Y. J. Dissolution and liquid crystals phase of 2D polymeric carbon nitride. *J. Am. Chem. Soc.* **2015**, *137*, 2179–2182.

[26] Yang, S. B.; Gong, Y. J.; Zhang, J. S.; Zhan, L.; Ma, L. L.; Fang, Z. Y.; Vajtai, R.; Wang, X. C.; Ajayan, P. M. Exfoliated graphitic carbon nitride nanosheets as efficient catalysts for hydrogen evolution under visible light. *Adv. Mater.* **2013**, *25*, 2452–2456.

[27] Fang, Y. X.; Flake, J. C. Electrochemical reduction of CO_2 at functionalized Au electrodes. *J. Am. Chem. Soc.* **2017**, *139*, 3399–3405.

[28] Nganga, J. K.; Samanamu, C. R.; Tanski, J. M.; Pacheco, C.; Saucedo, C.; Batista, V. S.; Grice, K. A.; Ertem, M. Z.; Angeles-Boza, A. M. Electrochemical reduction of CO_2 catalyzed by Re(pyridine-oxazoline)$(CO)_3$Cl complexes. *Inorg. Chem.* **2017**, *56*, 3214–3226.

[29] Wu, J. J.; Ma, S. C.; Sun, J.; Gold, J. I.; Tiwary, C.; Kim, B.; Zhu, L. Y.; Chopra, N.; Odeh, I. N.; Vajtai, R. et al. A metal-free electrocatalyst for carbon dioxide reduction to multi-carbon hydrocarbons and oxygenates. *Nat. Commun.* **2016**, *7*, 13869.

[30] Wu, J. J.; Yadav, R. M.; Liu, M. J.; Sharma, P. P.; Tiwary, C. S.; Ma, L. L.; Zou, X. L.; Zhou, X.-D.; Yakobson, B. I.; Lou, J. et al. Achieving highly efficient, selective, and stable CO_2 reduction on nitrogen-doped carbon nanotubes. *ACS Nano* **2015**, *9*, 5364–5371.

[31] Xu, J. Y.; Kan, Y. H.; Huang, R.; Zhang, B. S.; Wang, B. L.; Wu, K.-H.; Lin, Y. M.; Sun, X. Y.; Li, Q. F.; Centi, G. et al. Revealing the origin of activity in nitrogen-doped nano-carbons towards electrocatalytic reduction of carbon dioxide. *ChemSusChem* **2016**, *9*, 1085–1089.

[32] Liu, Y. M.; Chen, S.; Quan, X.; Yu, H. T. Efficient electrochemical reduction of carbon dioxide to acetate on nitrogen-doped nanodiamond. *J. Am. Chem. Soc.* **2015**, *137*, 11631–11636.

[33] Li, X.-H.; Wang, X. C.; Antonietti, M. Solvent-free and metal-free oxidation of toluene using O_2 and g-C_3N_4 with nanopores: Nanostructure boosts the catalytic selectivity. *ACS Catal.* **2012**, *2*, 2082–2086.

[34] Wang, X. C.; Maeda, K.; Chen, X. F.; Takanabe, K.; Domen, K.; Hou, Y. D.; Fu, X. Z.; Antonietti, M. Polymer semiconductors for artificial photosynthesis: Hydrogen evolution by mesoporous graphitic carbon nitride with visible light. *J. Am. Chem. Soc.* **2009**, *131*, 1680–1681.

[35] Li, Q.; Yang, J. P.; Feng, D.; Wu, Z. X.; Wu, Q. L.; Park, S. S.; Ha, C.-S.; Zhao, D. Y. Facile synthesis of porous carbon nitride spheres with hierarchical three-dimensional mesostructures for CO_2 capture. *Nano Res.* **2010**, *3*, 632–642.

[36] Li, X. C.; Wu, M.; Lai, Z. H.; He, F. Studies on nickel-based catalysts for carbon dioxide reforming of methane. *Appl. Catal. A: Gen.* **2005**, *290*, 81–86.

[37] Doyle, A. M.; Shaikhutdinov, S. K.; Jackson, S. D.; Freund, H.-J. Hydrogenation on metal surfaces: Why are nanoparticles more active than single crystals? *Angew. Chem., Int. Ed.* **2003**, *42*, 5240–5243.

[38] Zhang, J. S.; Zhang, M. W.; Yang, C.; Wang, X. C. Nanospherical carbon nitride frameworks with sharp edges accelerating charge collection and separation at a soft photocatalytic interface. *Adv. Mater.* **2014**, *26*, 4121–4126.

[39] Yu, H. J.; Shang, L.; Bian, T.; Shi, R.; Waterhouse, G. I. N.; Zhao, Y. F.; Zhou, C.; Wu, L.-Z.; Tung, C.-H.; Zhang, T. Nitrogen-doped porous carbon nanosheets templated from g-C_3N_4 as metal-free electrocatalysts for efficient oxygen reduction reaction. *Adv. Mater.* **2016**, *28*, 5080–5086.

[40] Li, Y. G.; Zhang, J.; Wang, Q. S.; Jin, Y. X.; Huang, D. H.; Cui, Q. L.; Zou, G. T. Nitrogen-rich carbon nitride hollow vessels: Synthesis, characterization, and their properties. *J. Phys. Chem. B* **2010**, *114*, 9429–9434.

[41] Lei, W. W.; Portehault, D.; Dimova, R.; Antonietti, M. Boron carbon nitride nanostructures from salt melts: Tunable water-soluble phosphors. *J. Am. Chem. Soc.* **2011**, *133*, 7121–7127.

[42] Bandi, A.; Kühne, H. M. Electrochemical reduction of carbon dioxide in water: Analysis of reaction mechanism on ruthenium-titanium-oxide. *J. Electrochem. Soc.* **1992**, *139*, 1605–1610.

[43] Eastwood, B. J.; Christensen, P. A.; Armstrong, R. D.; Bates, N. R. Electrochemical oxidation of a carbon black loaded polymer electrode in aqueous electrolytes. *J. Solid State Electrochem.* **1999**, *3*, 179–186.

[44] Tammeveski, K.; Arulepp, M.; Tenno, T.; Ferrater, C.; Claret, J. Oxygen electroreduction on titanium-supported thin Pt films in alkaline solution. *Electrochim. Acta* **1997**, *42*, 2961–2967.